

Original Research

A CaCO₃-based nanoplatform with sonodynamic and tumor microenvironment activated for combined *in vitro* cancer therapy

Jiale Cai ^a, Guiping Hu ^a, Lihua Hu ^b, Junge Chen ^a, Dan Chen ^a, Dan Liu ^a, Xiaolei Wang ^a, Boxian Hu ^a, Cheng Li ^{a,*}

^a Beijing Advanced Innovation Center for Biomedical Engineering, Beijing Advanced Innovation Center for Big Data-Based Precision Medicine, School of Engineering Medicine Beijing, Beihang University, Beijing 100191, China

^b Department of Cardiology, Peking University First Hospital, Beijing 100034, China

ARTICLE INFO

Keywords:

Sonodynamic therapy
Nitric oxide, CaCO₃
Tumor microenvironment
RNA-seq

ABSTRACT

Introduction: Sonodynamic therapy (SDT) has potential clinical applications for cancer therapy, and is yet restricted by complex tumor microenvironmental (TME) factors. Thus, the research problem of TME modulation as well as efficient tumor treatment still needs to be clarified.

Method: In this study, a calcium carbonate (CaCO₃) nanoplatform was designed for ultrasound (US) and TME response-triggered, which encapsulated Ag₂S and loaded with L-Arg, and further wrapped with RBC/Platelet membrane, named as QD@Ca/M_L-Arg.

Results: Non-invasive US-triggered SDT by Ag₂S and acidic environment-responsive drug release were achieved. *In vitro* experiments validated the efficacy of SDT, Ca-ion interference and nitric oxide (NO) gas therapy as combined therapy for cancer treatment. By means of RNA sequencing, the cancer therapeutic mechanism of SDT in redox-related pathways was elucidated. The immunosuppressive TME was simulated with a M2-macrophage/cancer cell co-culture system to confirm the immune activating effect of immunogenic cell death (ICD).

Conclusion: Accordingly, the potential of QD@Ca/M_L-Arg was demonstrated for *in vitro* TME modulation, cancer therapeutic efficacy and clinical translation.

Introduction

As one of the major causes of human health hazards, the incidence and mortality of cancer is increasing rapidly worldwide [1]. Due to the limitations of conventional therapies such as toxic effects of chemotherapy and difficulty in eradicating metastatic tumors, synthetic nanoparticles have been widely used in drug delivery studies of tumor [2]. Nanoscale drug delivery systems can be utilized to boost drug enrichment by optimizing the size, shape, and properties, thereby relieving the side effects of drugs and intensifying the therapeutic efficacy [3]. The main challenge of drug delivery in solid tumors is attributed to the complex state of the tumor microenvironment (TME) which promotes tumor growth, enhances tumor cell infiltration and metastasis and inhibits the efficacy of antitumor therapy [4].

The acidic extracellular pH state is a unique feature of TME [5]. Due to the high catabolic demand of the tumor, hypoxic tumor cells derive energy from glycolysis and convert glucose to lactate [6,7], thus creating an acidic state. This acidified pH gradient forms a physical barrier for

commonly used alkaline chemotherapeutic medicine [8,9]. Opportunities for pH-responsive nanoparticles in tumor diagnosis and treatment have also arisen due to the characteristic acidic TME [10]. Calcium-based nanoparticles, such as calcium carbonate (CaCO₃), calcium phosphate (CaP) and calcium peroxide (CaO₂), have received attention in cancer therapy by the facile synthesis, functionalized modifications and acidic degradation [11–14]. Jiawei Zhu et al. synthesized CaCO₃ nanoparticles doped with peroxidase and Chlorin e6 (Ce6) which present significant drug release in acidic TME (pH 6.0). Meanwhile the increased Ca²⁺ concentration disrupted the mitochondrial buffering capacity of calcium, leading to mitochondrial overloading, promoted the oxidative phosphorylation process and inhibited adenosine triphosphate (ATP) production, accelerated apoptosis of cancer cells [15].

Exogenous non-invasive stimulation or drug-controlled release means include light, sound, electricity, heat and magnetism [16–20], etc. The superiority of ultrasound (US) lies in the negligible invasiveness and deeper penetration depth of deep-sited tumors [21]. Sonodynamic

* Corresponding author.

E-mail address: li_cheng@buaa.edu.cn (C. Li).

therapy (SDT) refers to the irradiation of low-intensity US to sonosensitizers, which triggers generation of reactive oxygen species (ROS) [22]. High concentrations of ROS cause oxidative damage to cells, which is considered as a feasible solution to induce apoptosis or necrosis of cancer cells [23]. In particular, it was found in preclinical animal models and in preliminary clinical trial studies of breast cancer patients that tumor cell lysates induced by the SDT process can act as tumor antigens, thus eliciting antitumor immune reactions [24,25].

The hypoxic state of tumor limits the effectiveness of SDT with ROS as a therapeutic tool [26]. Various strategies have been promoted to alleviate tumor hypoxia, including delivering oxygen or synthetic nano-agents to the tumor region for curbing hypoxia [27–29]. Nitric oxide (NO) has become a trendy research issue as a vital molecular messenger associated with tumor intimately [30]. NO plays a crucial role in cancer formation and progression and reacts with ROS to produce peroxynitrite (ONOO^-) [31,32]. NO and ONOO^- with powerful nitrating and oxidizing skill to induce cell apoptosis and limit excessive mitochondrial respiration, thus inhibiting the expression of HIF-1 α in hypoxic tumor cells and alleviating tumor hypoxia [33–35].

In this study, an ultrasound and pH-responsive nanoparticles QD@Ca/M_L-Arg-for combining cancer therapy was developed (Fig. 1). Sodium alginate was operated as micelles for Ag_2S of oil-to-water phase transfer and template of acidic pH-degraded CaCO_3 mineralization layer. L-Arg-was loaded in the pores of CaCO_3 to generate NO under cellular synthase. The biocompatibility of the nanoparticles was improved by modifying the RBC/Platelet hybrid membrane. *In vitro* experiments demonstrated that efficient cancer therapy was achieved through QD@Ca/M_L-Arg-stimulated by US. Further, the role of NO gas therapy in regulating the hypoxic TME was investigated, and the immunosuppressive microenvironment remodeling of ICD was stimulated by SDT. This work presents a TME-regulable nanoparticles with effective combined therapy which might provide a novel insight to the cancer treatment.

Materials & method

Materials

Diethyldithiocarbamic acid silver salt (Ag (DDTC)), 1-Octadecene (ODE), 1-Dodecanethiol (DT), n-Hexane were purchased from Aladdin (ODE), 1-Dodecanethiol (DT), n-Hexane were purchased from Aladdin

Industrial Co., Ltd. (Shanghai, China). Acetone, sodium alginate, calcium chloride anhydrous, ammonium bicarbonate and potassium persulfate were acquired from Macklin Biochemical Co., Ltd. (Shanghai, China). L-Arginine (L-Arg), dimethyl sulfoxide (DMSO), 1,3-Diphenylisobenzofuran (DPBF), 2',7'-Dichlorofluorescein diacetate (DCFH-DA) were obtained from Sigma-Aldrich (St. Louis, MO, USA). The Cell Counting Kit-8 kit was purchased from Dojindo Laboratories (Kumamoto, Japan). DAF-FM DA, Fluo-4 AM, JC-1, Calcein AM/PI, DAPI and other cell fluorescence probes were all purchased from Beyotime Biotechnology (Shanghai, China). Matrigel, GSH test kit, Recombinant murine interleukin-4 (IL-4) and lipopolysaccharide (LPS) were provided by Solarbio (Beijing, China). Doxorubicin (Dox) was acquired from Amgicam Biomedical Co., Ltd. All the reagents mentioned above were at analytical grade and no purification was required for direct use.

Synthesis of QD, QD@Ca, QD@Ca_L-Arg

The synthesis method was adapted with reference to previous studies [36]. In a four-port flask, 76.8 mg diethyldithiocarbamic acid silver salt (Ag (DDTC)), 30 g 1-Octadecene and 6 g 1-Dodecane were added sequentially. Heating to 90 °C with vigorous stirring under anaerobic conditions by argon gas and maintaining the temperature for 10 min to remove water. Continue to heat up to 140 °C and keep it for 10 min till n-hexane quenching to terminate the reaction. Then adding acetone and centrifuging at 12,000 rpm/min for 10 min, the obtained Ag_2S is dispersed in n-hexane for subsequent experiments.

Weighing 50 mg sodium alginate dissolved in 20 mL of deionized water and 5 mg Ag_2S was added. Vigorously stirred and heated to 70 °C, the hexane was removed. Then 20 mg potassium persulfate was added to get deprotonated sodium alginate micelle solution. The $\text{Ag}_2\text{S}/\text{Alg}$ components were collected by centrifugation and redispersed in ethanol which contained 5 mg CaCl_2 to get Ca^{2+} coupled. The $\text{Ca}^{2+}\text{-Ag}_2\text{S}/\text{Alg}$ sections were placed in an airtight vacuum environment, with another beaker amidst of an appropriate amount of NH_4HCO_3 . The product of QD@Ca was collected by centrifugation at 8000 rpm/min for 10 min after 24 h [37].

10 mg QD@Ca was dispersed in 10 ml deionized water, 5 mg of L-arginine powder was added and stirred thoroughly at room temperature for 24 h. QD@Ca_L-Arg-was collected by centrifugation at 11,000 rpm/min for 10 min. The L-arginine loading rate was calculated by

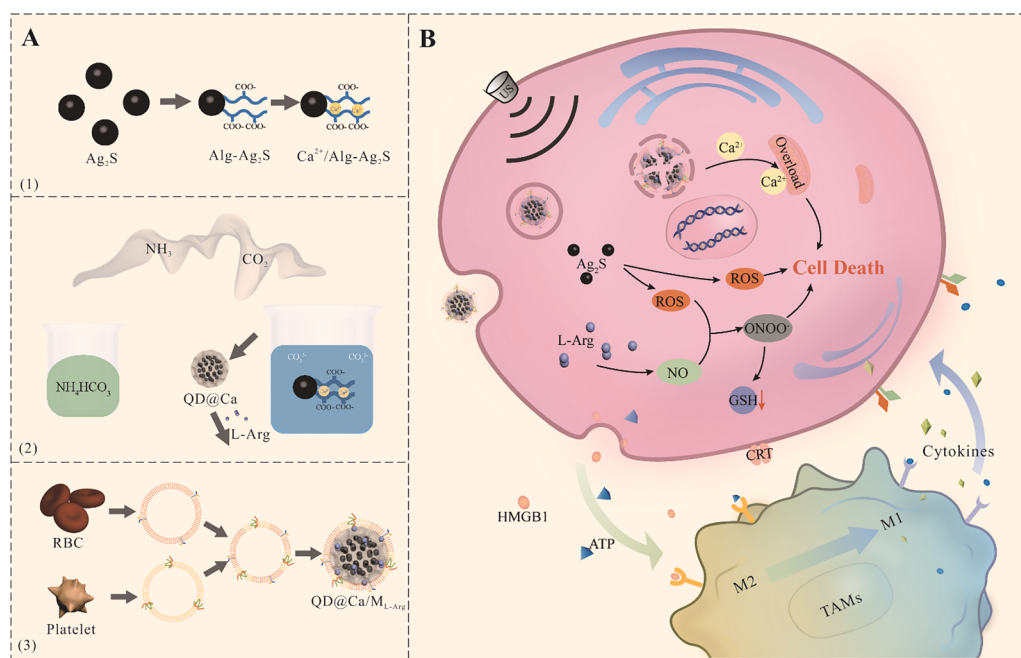


Fig. 1. Schematic illustration for the synthesis of QD@Ca/M_L-Arg-nano-particles: The synthesis was carried out in a three-step process, (1) sodium alginate was applied to convert oil-soluble Ag_2S quantum dots to water solubility; (2) sodium alginate was adopt as a template to obtain CaCO_3 mineralization layer; (3) RBC/Platelet heterozygous membrane manufactured biocompatibility (A); *In vitro* cancer therapy is executed in a cascade manner: exogenous US acts on QD@Ca/M_L-Arg to generate ROS; QD@Ca/M_L-Arg interpretation to releases L-Arg and Ca^{2+} , further realizing NO gas therapy and ion interference therapy; 4T1 cells develop ICDs which cause phenotypic conversion of TAMs (B).

α -naphthol-diacetyl reaction.

Synthesis of QD@Ca/M_L-Arg

Whole blood was obtained from male Balb/c mice and centrifuged at 3500 rpm/min for 5 min at 4 °C to remove the plasma. The RBCs were then lysed in an ice bath of 0.25 × PBS for 30 min. After centrifuging at 8000 rpm/min for 10 min, the RBCs ghost was resuspended in PBS at 4 °C.

Anticoagulated blood was added above the platelet isolation solution level at a ratio of 1:2. After centrifugation at 300 g for 15 min, the platelet plasma layer (first layer) was aspirated into another centrifuge tube, followed by the addition of the same volume of dedicated washing solution, washing 3 times. The platelets were stored in PBS at 4 °C.

The membrane coating was completed by fusing RBCs and platelet membrane with QD@Ca particles by ultrasonically maxing.

Characterization of QD@Ca/M_L-Arg

The morphology of the nanoscale drug delivery system was observed by JEM-2100 (JEOL, Japan) transmission electron microscope, with EDS accessory to determine the chemical elemental composition of it. Hydrodynamic diameters, zeta potential and polymer dispersity index were measured by Zeta Sizer (Malvern, UK). FTIR spectra were conducted on Nicolet 6700 FTIR spectrometer (Thermo scientific, USA). With NIRQUEST512-1.7 fiber spectrometer (Ocean Optics, USA) to record the near infrared fluorescence (NIR) spectra of Ag₂S, Alg/Ag₂S and QD@Ca. The UV-Vis absorption spectrum was conducted on BioMate 160 (Thermo scientific, USA).

Drug release study

The yield of ROS was quantified by DPBF. Under ultrasound, the absorbance at 410 nm of a mixture of DPBF and QD@Ca/M_L-Arg (75 µg/mL) solutions was detected every 1 min. DPBF and the mixture of DPBF + QD@Ca/M_L-Arg without ultrasound were regarded as control.

QD@Ca/M_L-Arg (3 mg) was dispersed in 3 mL PBS solution at pH 5.0, 6.5 and 7.4, respectively. Then, the supernatant was collected by centrifugation at a predetermined time and supplemented with the same volume of PBS of corresponding pH to the original solution. The cumulative release of Ca²⁺ was calculated by Calcium Assay Kit (Nanjing Jiancheng).

The release of L-Arg was determined by α -naphthol-diacetyl reaction. Specifically, the indicator contains 40 mg/mL NaOH hydroxide solution, 80 mg/mL α -naphthol and 0.5 µL/mL diacetyl both dissolved in propanol, the three solutions are mixed in equal volume. 130 µL of indicator was mixed with 20 µL supernatant and the mixture was water bathed at 30 °C for 15 min. Measure the absorbance at 540 nm.

Cell culture and treatment

RAW264.7 mouse macrophage and 4T1 mouse breast cancer cells were cultured in RPMI 1640 medium containing 10% FBS; MDA-MB-231 human breast cancer cells were cultured in DMEM medium containing 10% FBS. The cells mentioned above were nurtured in a 37 °C incubator with 5% CO₂.

Biocompatibility and endocytosis

Cells in logarithmic growth phase were inoculated in 96-well plates at a density of 1 × 10⁵ cells per mL overnight at 37 °C and incubated with gradient concentrations of QD@Ca/M_L-Arg, CaCO₃, and Ag₂S (0, 3.125, 6.25, 12.5, 25, 50, 100 µg/mL) for 24 h. 10 uL CCK-8 was added into each well, the absorbance was measured at 490 nm to calculate cell viability.

4T1 cells (1 × 10⁵/mL) were inoculated and grown overnight in

confocal dishes at 37 °C. Replacing the medium by Dil marked QD@Ca/M_L-Arg for incubation of 4 h. Immobilizing 4T1 cells with cell fixation solution for 20 min, the images were observed by confocal laser scanning microscopy (Dragonfly, UK).

Chemotherapy drug therapy research

Doxorubicin (Dox) was selected as a typical chemotherapy drug for breast cancer cell chemical treatment.

MDA-MB-231 and 4T1 cells were seeded in 96-well plates at a density of 1 × 10⁵ cells per mL. After incubated overnight at 37 °C, gradient concentrations of Dox (0, 0.125, 0.25, 0.5, 1, 2, 4 and 8 µg/mL) were added for another 12 h. 10µL CCK-8 was added into each well, the absorbance was measured at 490 nm to calculate cell viability.

Scratch assay and migration assay

MDA-MB-231 and 4T1 cells were seeded into 6-well plates to reach a dense monolayer, and a uniform scratch was made. After washing off the shedding cells with PBS, the medium was replaced by QD@Ca/ML-Arg (75 µg/mL). With incubation for 4 h, cells were irradiated with US (1 W/cm², 2–3 min). The pictures were taken at 0 h, 24 h and 48 h after treatment. The distances of the wound field were processed by ImageJ software.

Cell culture inserts (8 µm PET membrane, Corning) upper surface were wrapped with Matrigel (200 µg/mL). For cells pre-treated by QD@Ca/M_L-Arg+US, 4T1 cells were resuspended with FBS-free medium and seeded into inserts. 600 uL RPMI 1640/10% FBS was added as chemotactic factor in the lower chamber. After incubating at 37 °C for 48 h, wiping off the Matrigel and cells in the inserts and staining the inserts with 0.1% crystal violet for 20 min. Crystal violet was dissolved by 33% acetic acid and absorbance readings were taken at 570 nm.

Detection of in vitro ROS and NO

4T1 cells were inoculated in confocal dishes and cultured overnight, FBS-free medium containing QD@Ca/M_L-Arg (75 µg/mL) was added for 4 h. The cells were then incubated with DCFH-DA (10 µM) and DAF-FM DA (5 µM). After imposed with US (1 W/cm², 2 min). The fluorescence was obtained by CLSM.

In vitro ONOO⁻ generation and GSH depletion

4T1 cells were cultured to the experimentally desired density, replaced the medium with L-Arg (50 µg/mL) or QD@Ca/M_L-Arg (75 µg/mL) for incubating another 4 h. The ONOO⁻ probe (BBoxiProbe, BB-460,652) was utilized to detect peroxynitrite after irradiation of US (1 W/cm², 2 min).

4T1 cells were cultured overnight. Replacing the medium with L-Arg (50 µg/mL) or QD@Ca/M_L-Arg (75 µg/mL) for incubating another 4 h. 5,5'-dithiobis-(2-nitrobenzoic acid) (DTNB) assay kit obtained the content of intracellular GSH.

Ca²⁺ detection and mitochondrial membrane potential measurement

4T1 cells were cultured at 37 °C for 24 h. Then, QD@Ca/M_L-Arg (75 µg/mL) was added. After incubated with Fluo-4 AM (2 µM) for 30 min, the images were obtained by CLSM at scheduled time point (0, 0.5, 1 and 2 h).

4T1 cells were inoculated in confocal dishes and cultured overnight, replaced the medium with CaCO₃ or QD@Ca/M_L-Arg for incubating another 4 h. Then the cells were exposed to US for 2 min (1 W/cm²) and stained with mitochondrial membrane potential probe (JC-1).

Immunofluorescence staining

For immunofluorescence staining, 4T1 cells pre-seeded in a 6-well plate were incubated overnight. After the aforementioned incubation with QD@Ca/M_L-Arg and treatment by US, immobilizing 4T1 cells with cell fixation solution for 20 min. With blocking buffer to get cells blocked and permeabilized for 1 h. Stained cells with antibody (anti-HIF-1 α , anti- γ -H₂AX and anti-CRT, respectively) overnight at 4 °C and subsequently secondary anti-rabbit AlexaFluor-555 for 1 h, and then counter-stained with DAPI for 10 min.

In vitro efficacy of combined therapy

4T1 and MDA-MB-231 cells were cultured to the experimentally desired density, the medium was replaced by QD@Ca/M_L-Arg (75 μ g/mL) in FBS-free medium. Cells were irradiated with US afterwards. Operating Calcein AM/PI cytotoxicity assay kit and CCK-8 to evaluate the combined efficacy.

Study of DAMPs release

4T1 cells were seeded into 6-well plates and incubated overnight. After incubation with probes and treatment by US, the level of calretinin (CRT) was identified by immunofluorescence. The concentration of HMGB1 and ATP was qualified by ELISA kits (FeimoBio) and ATP assay kit (Beyotime) respectively.

RNA-sequencing analysis

To clarify the genetic variation by combined therapy, the mRNA was isolated by Trizol reagent (Invitrogen). RNA-seq was conducted on Illumina platform, transcript levels were quantized using featureCounts. Differential expression between two comparative groups was performed using DESeq2 software. GO/KEGG enrichment analysis was achieved by ClusterProfiler R software. Based on the STRING database predicted protein-protein interactions.

Cell viability and cytokines levels in coculture system

200 μ L Raw264.7 cells were seeded in the upper chamber of the cell culture inserts (0.4 μ m PET membrane, Corning), with LPS (1 μ g/mL) or IL-4 (25 ng/mL) treated to achieve M1 or M2 TAMs phenotype respectively. 600 μ 4T1 cells were cultured in the lower chamber, incubated with probes and treated by US subsequently. The 4T1 cells were collected by trypsin at scheduled time for viability measurement by CCK-8. IL-6, IL-10 and TNF- α were quantified by ELISA kits for cytokine detection.

Statistical analysis

The data was analyzed by GraphPad Prism 7.0 software and presented as mean \pm standard deviation. Statistical comparisons were assessed by one-way ANOVA. Taken P values < 0.05 as accepted level of significance.

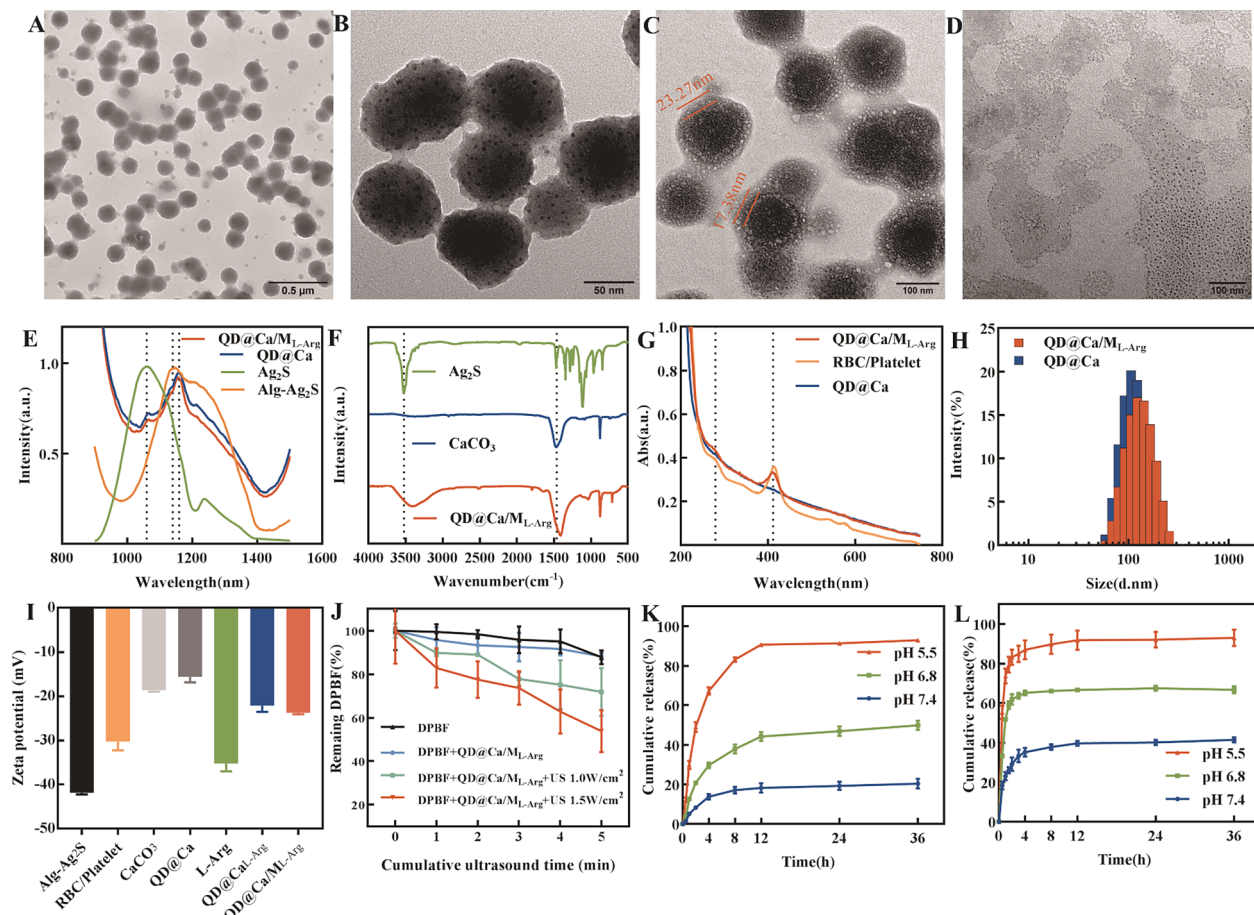


Fig. 2. TEM images of QD@Ca (A and B), QD@Ca/M_L-Arg (C), and the degradation of QD@Ca/M_L-Arg in PBS at pH 6.8 for 4 h (D); fluorescence spectra (E), FTIR (F) and UV-vis (G) of different nanoparticles; hydrated particle size (H) and zeta potential (I) change after coated with RBC/Platelet vesicles and loaded by L-Arg; ROS production was detected by DPBF (J); the release of Ca²⁺ (K) and L-Arg (L) of QD@Ca/M_L-Arg at different pH conditions.

Results

Synthesis and characterization of QD@Ca/M_L-Arg

In this study, oil-soluble Ag₂S QDs were synthesized to accomplish SDT by pyrolysis, and then dispersed in sodium alginate micelles. Sodium alginate wrapped Ag₂S through hydrogen bonding and hydrophobic interactions to obtain water-soluble Alg/Ag₂S polymers [38]. Then, QD@Ca nanoparticles were obtained through calcium carbonate deposited on Ag₂S by gas diffusion with a size of about 100 nm (Fig. 2A

and B). The RBC/Platelet vesicles modified nanoparticles showed a distinct shell-core structure with a slight increase in size of about 120 nm (Fig. 2C) which promoted water solubility of QD@Ca.

The emission peak of Ag₂S QDs appeared at 1050 nm under laser excitation of 808 nm, present in fluorescence spectrum. The peak emerged with a different degree of red-shift after calcium carbonate depositing and vesicles modifying (Fig. 2E). As shown in the fourier transform infrared spectroscopy (FTIR), the typical absorption bands at 3551 cm⁻¹ and 1456 cm⁻¹ were related to the hydroxyl stretching vibration and carbonate ion respectively (Fig. 2F) [39,40]. UV-vis

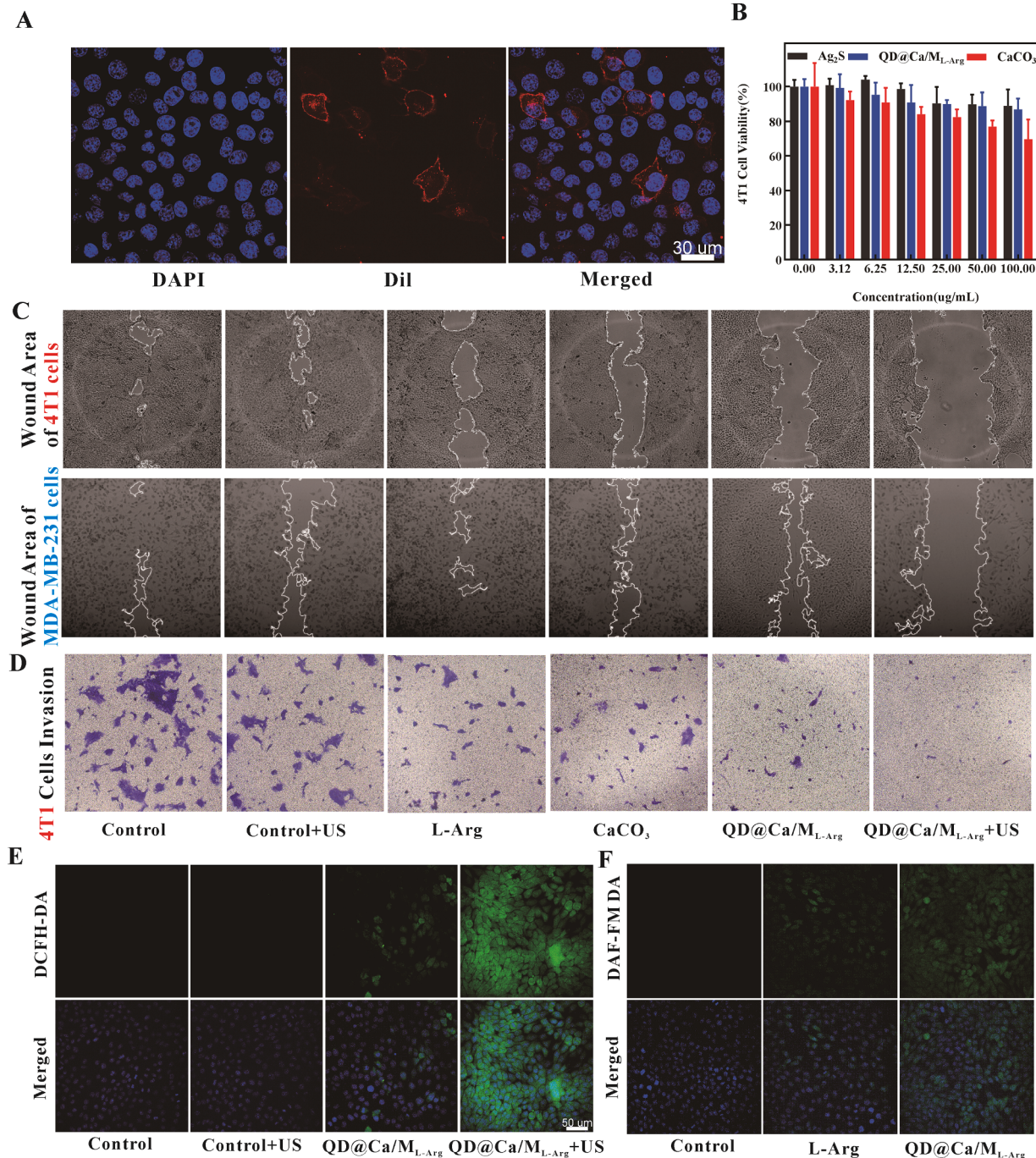


Fig. 3. Confocal fluorescence images of 4T1 cells incubated with Dil-QD@Ca/M_L-Arg (A); The relative 4T1 cell viabilities after treated with different nanoparticles of gradient concentrations (B); 4T1 and MDA-MB-231 cells' migration (C) and invasion (D) after different treatment; intracellular ROS (E) and NO (F) production was detected by DCFH-DA and DAF-FM DA, respectively; Confocal fluorescence images of ONOO⁻ (G); the intracellular GSH concentration of hypoxic 4T1 cells after different treatment (H); the immunofluorescence images of HIF-1α (I) and γ-H2AX (J) after treated with QD@Ca/ML-Arg-and US. n.s.: no significant, *P < 0.05, ***P < 0.001.

absorbance spectrum displayed the characteristic absorption peaks of QD@Ca/M_L-Arg-at 290 nm and 410 nm which matched the RBC/Platelet vesicles (Fig. 2G). And the loading rate and encapsulation efficiency of L-Arg-were calculated to be 11.33 ± 0.81% and 45.32 ± 3.23% by α-naphthol-diacetyl reaction [41].

Energy Dispersive Spectrometer (EDS) confirmed the presence of elemental composition in QD@Ca/M_L-Arg (Table S1). Comparing the hydrodynamic particle size and the surface potential of QD@Ca with/without modification by membrane, the size increased from 105 to 122 nm (Fig. 2H). And shown a negative potential of -23 mV due to the membrane proteins and L-Arg (Fig. 2I). In addition, the stability of the nanoparticle is the primary mission to consider. QD@Ca/M_L-Arg-was examined in PBS, water and RPMI 1640 medium (10% FBS), at different temperatures. There were no significant changes in size, polydispersity index (PDI) and surface potential over four days, indicating that QD@Ca/M_L-Arg-has outstanding physiological stability (Fig. S1).

To assess the sonodynamic performance of QD@Ca/M_L-Arg, 1,3-diphenylisobenzofuran (DPBF) was used as ROS quantitative probe. The absorption of DPBF shows a reduction after exposure to US, which indicates the ROS generation by Ag₂S under US excitation (Fig. 2J).

It has extensively known that CaCO₃-based nanomaterials have classical pH-sensitive degrade property. The TEM Figure exhibits QD@Ca/M_L-Arg-disintegrated and enlarged in PBS at pH 6.8 for 4 h (Fig. 2D). To substantiate the drug release in acidic TME, Ca²⁺ and L-Arg-in PBS with different pH values were evaluated. Ca²⁺ had a pH acid-dependent increase with duration of incubation, demonstrating the acid degradation ability of the synthetic nanoparticles (Fig. 2K). Similarly, the release of L-Arg-was calculated by α-naphthol-diacetyl reaction. In PBS of pH 5.5, 86.92 ± 4.12% of L-Arg-being released within 4 h. In contrast, in the PBS of pH 7.4, only 35.16 ± 0.82% of L-Arg-was released during the same time (Fig. 2L).

Functions of QD@Ca/M_L-Arg

RBC/Platelet vesicles confer excellent biocompatibility to QD@Ca/M_L-Arg, thus avoiding immune clearance and achieving more intratumorally drug delivery. To Figure out the intracellular uptake process, the Dil marked QD@Ca/M_L-Arg-was incubated with 4T1 cells first. As shown in Fig. 3A, Dil-QD@Ca/M_L-Arg-could be internalized via endocytosis and scattered in cytoplasm effectively.

Nanoscale drug delivery systems with great biocompatibility are essential to promote their biomedical applications. CaCO₃, Ag₂S, L-Arg-and QD@Ca/M_L-Arg-displayed inappreciable toxicity to 4T1 cells after 24 h of incubation. With concentrations of QD@Ca/M_L-Arg-up to 100 μg/mL, 4T1 cells incubated by QD@Ca/M_L-Arg-remained 88.97 ± 6.24% of survival rate. For L-Arg, Ag₂S and CaCO₃, cells also maintained 93.17 ± 0.34%, 87.93 ± 9.39% and 69.60 ± 11.43% relative viability, respectively (Fig. 3B). After co-incubation with RBCs for 12 h, only negligible hemolysis was present in QD@Ca/M_L-Arg-group (Fig. S2).

Performing wound healing test to simulate the process of metastatic breast cancer cells migration *in vitro*. 4T1 cells were cultivated as a monolayer and created a “wound scratch” (Fig. S3). The control group healed most with the healing rate of 82.93 ± 0.89% after 48 h. Only US treatment as well as free L-Arg-and CaCO₃ achieved a limited inhibitory effect. The considerable migration inhibition was accomplished by QD@Ca/M_L-Arg+US, with a healing rate of only 13.11 ± 12.09% (Fig. 3C). The parallel results were also demonstrated in the MDA-MB-231 cell line. Compared to the high healing rate of 84.23 ± 1.19% in the control group, the healing rate in the QD@Ca/M_L-Arg+US group was only 12.88 ± 3.94% after 48 h (Fig. 3C and Fig. S5). Similarly, the longitudinal metastasis and invasion of 4T1 cells was simulated by transwell with Matrigel. Only US treatment, free L-Arg-and CaCO₃ were unable to inhibit cell invasion, analogous to wound healing test. QD@Ca/M_L-Arg+US had the highest invasion inhibition rate of 74.01 ± 3.26% (Fig. 3D and S4).

Fluorescence imaging displayed hardly ROS was generated with only

US treatment or QD@Ca/M_L-Arg-incubation. The 4T1 cells treated with QD@Ca/M_L-Arg-under US presented enormous ROS generation (Fig. 3E and S6 A). Correspondingly, extensive NO was detected in the 4T1 cells of QD@Ca/M_L-Arg-group (Fig. 3F) while free L-Arg-failed to produce large amount of NO. Speculation is that QD@Ca/M_L-Arg-enhanced the intracellular delivery of L-Arg. Further, the intracellular NO level was measured by the classical Griess method and mutually corroborating to the fluorescence image (Fig. S6 B), which revealed the same trend as fluorescence images of NO.

The intracellular ONOO⁻ level was also analyzed. As shown in Fig. 4A, the free L-Arg-group did not produce ONOO⁻. The strongest fluorescence, which is obtained from the reaction between ROS and NO generated by QD@Ca/M_L-Arg+US. Cancer counteract PDT or SDT using ROS as a therapeutic tool by increasing the content of endogenous glutathione (GSH). It was found that ONOO⁻ inhibit GSH levels by modulating GSH-related synthase through the nitration reaction. Intracellular GSH content was measured by DTNB kit and significantly reduced by ONOO⁻ in the QD@Ca/M_L-Arg+US group (Fig. 4B).

It has been reported that NO and ONOO⁻ could regulate HIF-1α transcription, thereby overcoming drug resistance of tumor due to hypoxia. As revealed in Fig. 4C, which insinuate QD@Ca/M_L-Arg+US has the potential to down-regulate the expression of HIF-1α by releasing ONOO⁻ in hypoxic 4T1 cells. Considering the generation of ROS and ONOO⁻ under US, the DNA damage status was investigated by immunofluorescence staining of γ-H₂AX. Strongest fluorescence was observed in QD@Ca/M_L-Arg+US group (Fig. 4D), which speculated that DNA damage by generating ROS and possibly indicates that DNA self-restoration was impeded by ONOO⁻. Relevant quantitative results were reflected in Figure S7.

Efficacy of combined therapy against cancer cells

Due to the degrade of CaCO₃-based nanoplatform in acid environment. Intracellular Ca²⁺ content was assessed by the Ca²⁺ fluorescent probe Fluo-4 AM (Fig. S8). A time-dependent increase of Ca²⁺ was observed within 2 h due to the degradation of QD@Ca/M_L-Arg-by lysosome through the endocytic pathway (Fig. 5A). Mitochondria are crucial organelles for the regulation of cellular respiration and intracellular calcium homeostasis, while accumulation of Ca²⁺ is harmful for mitochondria function. The mitochondrial damage was evaluated by the mitochondrial membrane potential fluorescence probe (JC-1). Fig. 5B and S9 showed a high level of mitochondrial red fluorescence of control group, which indicates that 4T1 cells maintain high mitochondrial activity. After incubation with QD@Ca/M_L-Arg, green fluorescence of reduced membrane potential was emerged in 4T1 cells. Normal mitochondrial membrane potential is the premise of maintaining mitochondria for oxidative phosphorylation and ATP production, which is necessary for maintaining cell function. The mitochondrial membrane potential decline is an early sign of tumor cell apoptosis, which indicates the amplification of the oxidative stress state of the mitochondria by the ROS generated by SDT.

Immunogenic cell death (ICD) is a specialized form of cell death which can be triggered by SDT. Cancer cells that undergo ICD can initiate an adaptive immune response and establish a long-term immune response, thereby obtaining anti-tumor immunity. ICD is characterized by the release of damage associated molecular patterns (DAMPs), including adenosine triphosphate (ATP), high mobility group protein B1 (HMGB1), and calprotectin (CRT) [42]. CRT migrates from the endoplasmic reticulum to the surface of the cell membrane and provides an “eat-me” signal for dendritic cell uptake. The immunofluorescence image of CRT showed that neither US nor synthetic nanoparticles treatment alone could trigger the migration of CRT, while QD@Ca/M_L-Arg+US group brought the highest level of CRT fluorescence detected on the surface of 4T1 cells (Fig. 5C). Similarly, the release of ATP and HMGB1 provided additional antigen stimuli for immunocytes maturation, which was evaluated respectively. Obviously,

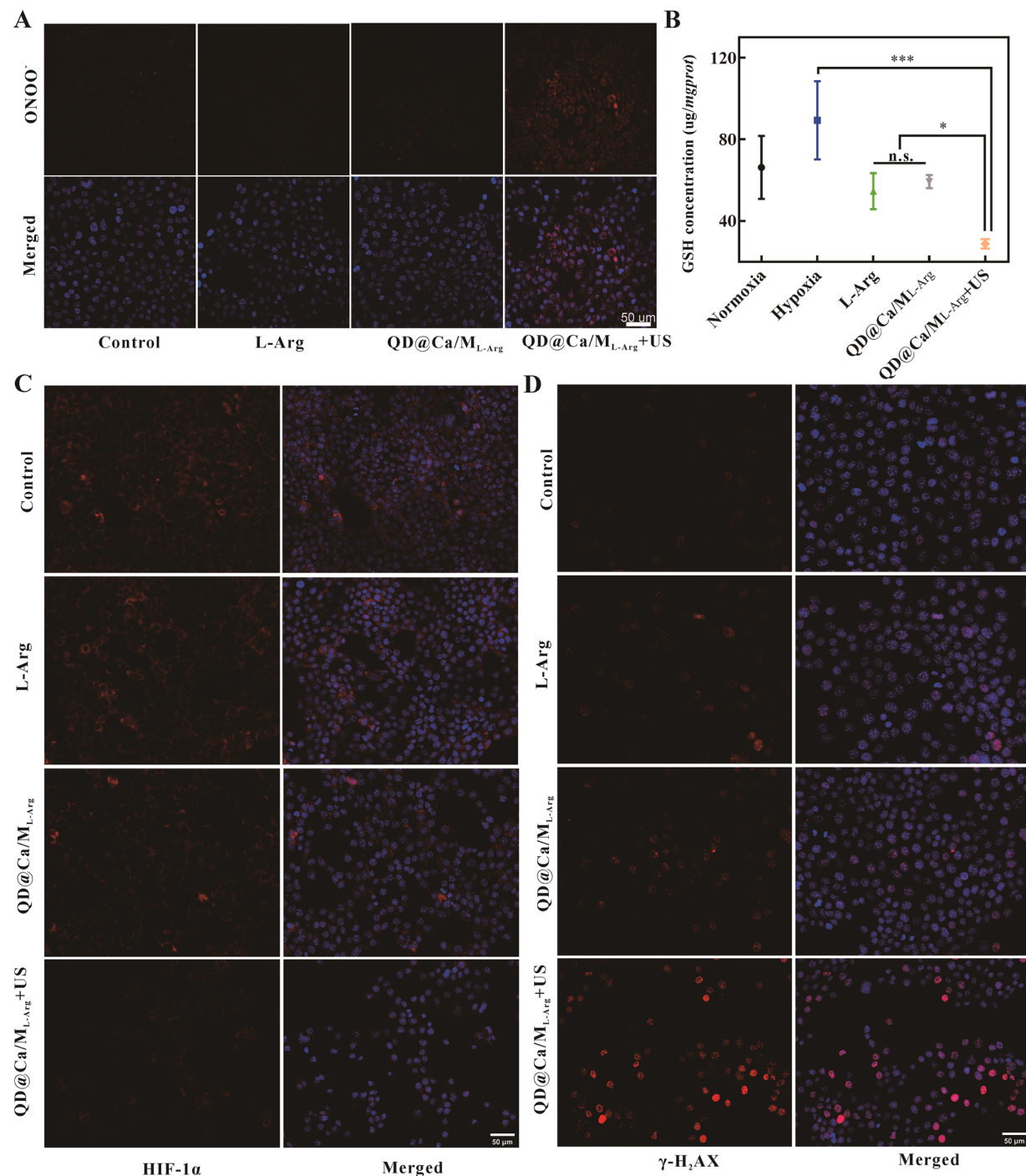


Fig. 4. Confocal fluorescence images of ONOO- (A); the intracellular GSH concentration of hypoxic 4T1 cells after different treatment (B); the immunofluorescence images of HIF-1 α (C) and γ -H₂AX (D) after treated with QD@Ca/ML-Arg-and US. n.s.: no significant, *P < 0.05, ***P < 0.001.

QD@Ca/M_{L-Arg}+US caused the highest extracellular drain of ATP and HMGB1, demonstrating the ICD effect (Fig. 5D-E and Fig S9).

To validate the US-triggered combined therapy of synthetic nanoparticle, neither CaCO₃, L-Arg-nor Ag₂S without US-triggered produced therapeutic effects on 4T1 cells, as previously result shown (Fig. 3B). CaCO₃L-Arg-and Ag₂S, Ag₂S_{L-Arg}, QD@Ca treated with US, namely SDT, Ca-ion interference and NO gas therapy, as a single treatment or a combination of two factors, could not kill 4T1 cancer cells adequately (Fig. S10). Further, the efficacy of combined therapy was verified by Calcein AM/PI staining and relative viability calculation of 4T1 cells. Fluorescence imaging of Fig. 6A showed that, the 4T1 cells incubation with QD@Ca/M_{L-Arg} keeping alive. Whereas QD@Ca/M_{L-Arg}+US group

present large amount of red fluorescence which indicated the reduced activity of 4T1 cells through cascade treatment reactions generated by QD@Ca/M_{L-Arg} under US irradiation. The cell viability quantification using CCK-8 assay kit, the relative viability of 4T1 cells under the combined therapy was only 58.26 ± 6.17%, which validated the combination therapy produced a strong therapeutic effect on cancer cells (Fig. 6B). Similarly, the therapeutic efficacy verification in the MDA-MB-231 cell line was conducted. Results showed that QD@Ca/M_{L-Arg}+US group produced considerable reduced activity (Fig. 6D) in MDA-MB-231 cells, with a survival rate of only 53.05 ± 11.75% (Fig. 6E).

To verify the synthesized nanoscale drug delivery system whether or not present more effective therapeutic capabilities, a typical

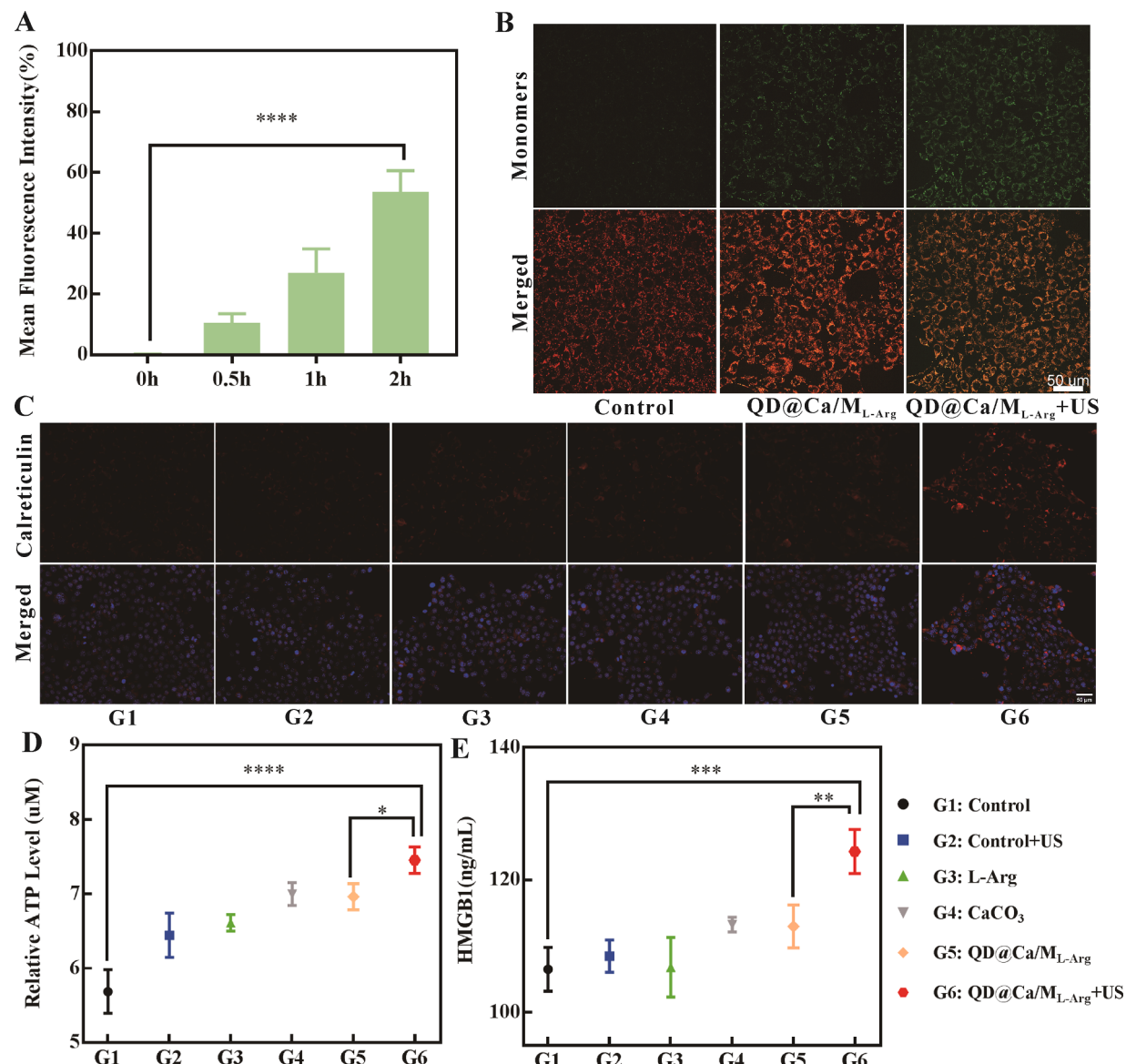


Fig. 5. Intracellular Ca^{2+} was assessed by Fluo-4 AM (A); the mitochondrial membrane potential was acquired by JC-1 (B); the DAMPs detection of CRT (C), ATP (D) and HMGB1 (E).

chemotherapy drug doxorubicin (Dox) was selected and performed at gradient concentration on 4T1 cells and MDA-MB-231 cell lines. The results displayed that at the concentrations of 4 $\mu\text{g}/\text{mL}$, the viability of the two cell lines decreases to $44.08 \pm 2.46\%$ and $55.18 \pm 3.19\%$ respectively (Fig. 6C and F). Although traditional chemotherapy seems to be an effective treatment, the ensuing toxic side effects on normal tissues cannot be ignored. The nanoscale drug delivery system designed and synthesized in this experiment realized the sonodynamic combined therapeutic effect triggered by exogenous ultrasound. As shown in Fig. 3B, no significant cytotoxicity was produced when ultrasound was not administered, which reflects the specific therapeutic characteristics of ultrasound-guided.

Reprogramming of M2 to M1 TAMs by ICD

M2-type macrophages resisting immune activity and increasing resistance to chemotherapeutic agents. Reprogramming from suppressive to promoting immune microenvironment is emerging as a novel tool [43]. Raw 264.7 cell lines are capable of typical TAMs phenotype transformation *in vitro*, which were employed as a simulated

inflammatory cell model here. The phenotype (M0, M1 and M2) was established firstly, and similar to the previous section, cell survival ratio was assessed after administration of different nanoparticles to tumor-associated macrophages (TAMs). None of the nanoparticles produced significant cytotoxicity to TAMs (Fig. S11).

To investigate the reprogramming of TAMs, L-Arg, CaCO₃, and QD@Ca/M_{L-Arg} was administered to M2 TAMs respectively, and applied US. Cytokines secreted by M2 TAMs were collected and quantified for enzyme-linked immunosorbent assay (ELISA). None of the stimuli could transfer M2 to M1 phenotype, i.e., the increment of proinflammatory cytokines (IL-6) and reduction of anti-inflammatory cytokine (IL-10) (Fig. 7A and B).

Inspired by previous studies that ICD-induced DAMPs release could activate the anti-tumor immune function, the co-culture model of 4T1 and M2 cells was established. The lower chamber inoculated with 4T1 and M2 cells and administered by QD@Ca/M_{L-Arg} as well as US treatment, with M2 TAMs cultivated in the upper inserts. As shown in Fig. 7A and B, QD@Ca/M_{L-Arg}+US acting on 4T1 cancer cells increased IL-6 and decreased IL-10 level.

To determine the phenotypic switch was generated by ICD, 4T1 and

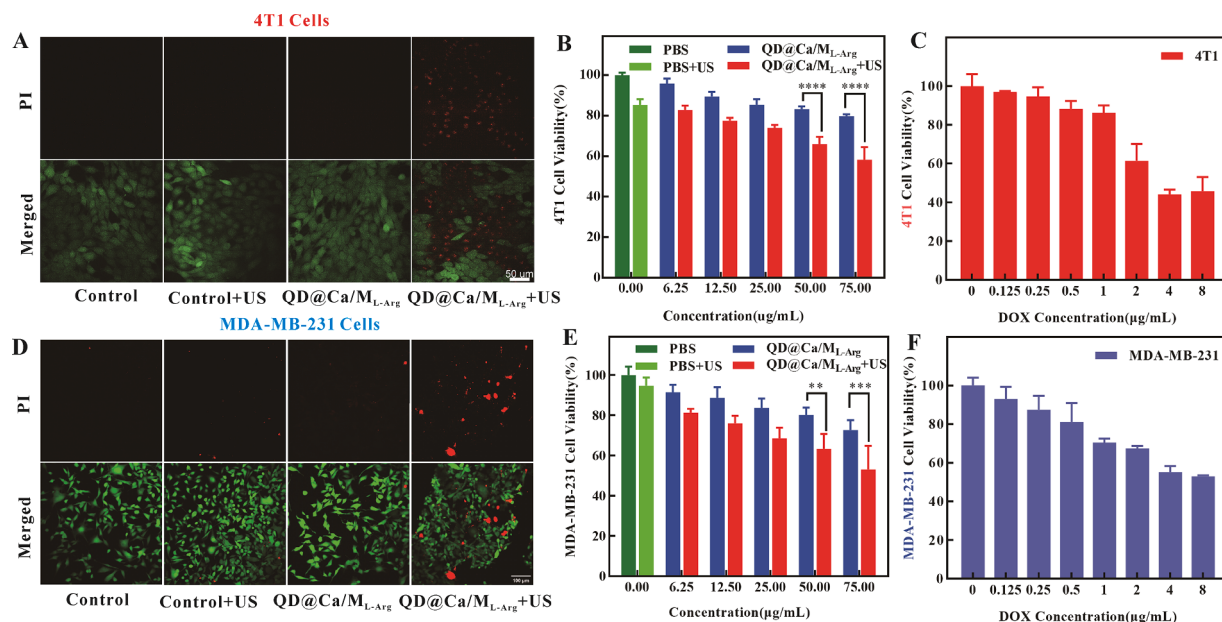


Fig. 6. Calcein AM/PI staining of 4T1 cells incubated with QD@Ca/M_L-Arg and irradiated by US (F) and quantified by CCK-8 kit (G); Calcein AM/PI staining of MDA-MB-231 cells incubated with QD@Ca/M_L-Arg and irradiated by US (H) and quantified by CCK-8 kit (I). *P < 0.05, **P < 0.01, ***P < 0.001, ****P < 0.0001.

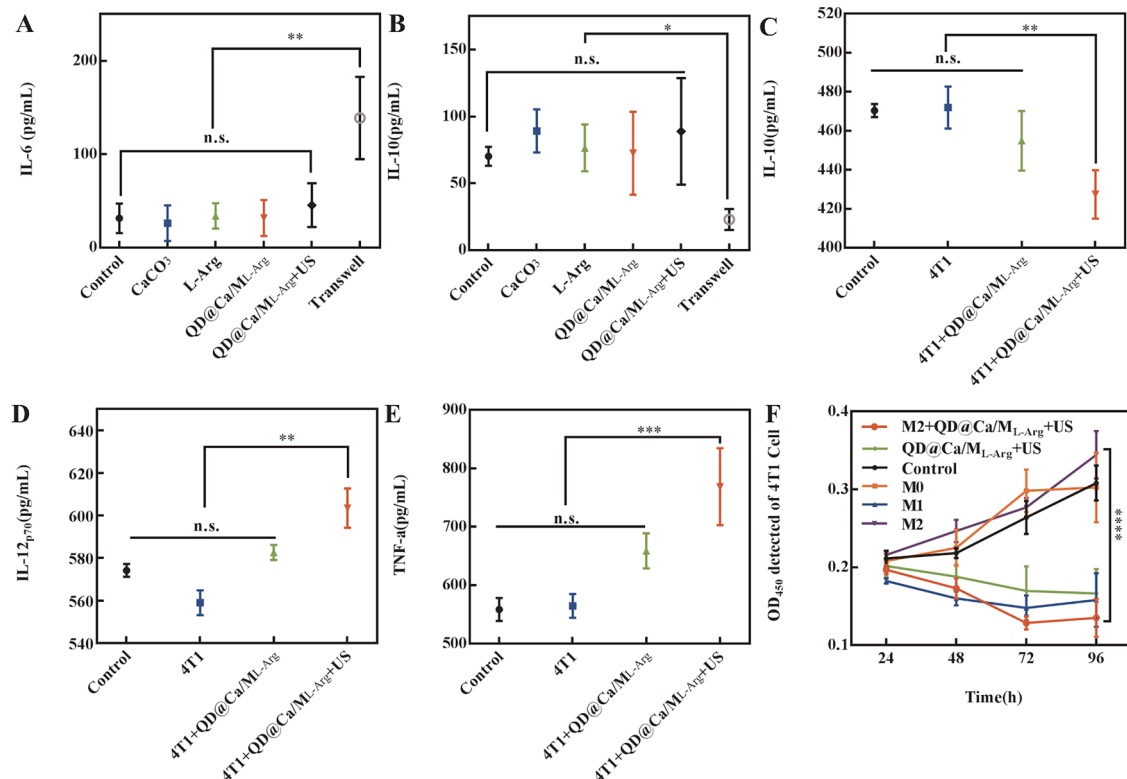


Fig. 7. The IL-6 (A) and IL-10 (B) generation was measured by ELISA kit after incubating with different nanoparticles; the cytokines of IL-10 (C), IL-12_{p70} (D) and TNF-α (E) was collected in tranwell inserts and detected by ELISA; the OD value was measured of 4T1 cells of co-cultured transwell system after incubated with CCK-8 (F).

M2 co-culture model with different treatments was analyzed. Results exhibited hardly M1 phenotypic switch (IL-10, IL-12, TNF-α) within the 4T1 cells and another group of 4T1 cells incubated by QD@Ca/M_L-Arg without US. Consequently, determined that QD@Ca/M_L-Arg+US not only kills cancer cells, but triggers ICD to release DAMPs which induces reprogramming in macrophages (Fig. 7C-E).

Based on the TAMs reprogramming, the immune effect was

evaluated. As results presented in Fig. 7F, the OD value detected at 450 nm reflected of a phenomenon that M2 TAMs were able to promote cancer cell proliferation, and M1 TAMs as well as QD@Ca/M_L-Arg+US had the ability to partially inhibit the growth of cancer cells. Simultaneously, QD@Ca/M_L-Arg+US activated the phenotypic switch from M2 to M1, preventing the proliferation of 4T1 cancer cells.

RNA-seq analysis

To demonstrate the mechanism of cytotoxicity produced by US activation of QD@Ca/M_L-Arg-on 4T1 cells, whole genome transcriptome sequencing analysis was inspected of 4T1 cells incubated by QD@Ca/M_L-Arg-with/without US treatment [44]. A total of 12,394 genes were examined for transcription during this test. Quantitative Venn diagram revealed that 225 genes were transcribed exclusively in QD@Ca/M_L-Arg-treated 4T1 cells; 205 genes were transcribed particularly in QD@Ca/M_L-Arg+US-treated cells (Fig. 8A). The genic expression data were statistically analyzed and visually demonstrated using volcano plots. Compared with Control group, 4118 genes were upregulated, and 4140 genes were downregulated in QD@Ca/M_L-Arg+US-treated cells; with 4286 genes were upregulated and 4321 genes were downregulated in QD@Ca/M_L-Arg-treated cells. Compared with QD@Ca/M_L-Arg-group, 2157 genes were upregulated, and 2052 genes were downregulated in QD@Ca/M_L-Arg+US-treated cells (Fig. 8B).

Gene Ontology (GO) enrichment was applied to describe the gene functions. Taking QD@Ca/M_L-Arg-as an example, QD@Ca/M_L-Arg+US treatment exerted remarkable effects on 4T1 cells in terms of mitotic cell cycle, mitochondrial inner membrane and calmodulin binding (Fig. S12), etc. Kyoto Encyclopedia of Genes and Genomes (KEGG) enrichment analysis is a comprehensive database integrating genomic, chemical and phylogenetic function. Specifically, 4T1 cells treated with QD@Ca/M_L-Arg+US, involved in signaling pathways such as p53, HIF-1, FoxO, ErbB, and oxidative phosphorylation were significantly affected, compared with Control group (Fig. 8C).

Further mining of gene clustering heat map, found that the HIF-1-

related pathway had a significant trend of inhibited expression in the QD@Ca/M_L-Arg+US group, which was consistent with the pattern of HIF-1 α in hypoxic cancer cells that was suppressed by ONOO⁻ in the previous report. For the Ras/Raf/Mek/Erk signaling pathway with characterized genes such as Ephb2, Ephal1 and Bmp1, the 4T1 cells treated by QD@Ca/M_L-Arg+US appeared significant discrepancy compared with incubated by QD@Ca/M_L-Arg-only. Which predicts a possible cancer cells' therapeutic effect produced of ROS by SDT. With the key role APAF1 gene performed in mitochondrial apoptosis, and the higher activation of APAF1 gene in the QD@Ca/M_L-Arg+US and QD@Ca/M_L-Arg-group demonstrated Ca²⁺-mediated mitochondrial overload. The resulting activation of apoptotic genes such as Casp-1, Casp-3 and Casp-9 revealed cancer cell death induced by combined therapy (Fig. 8D). The protein-protein interaction (PPI) network depicts the potential interactions of genes mentioned above (Fig. 8E).

Conclusion and discussion

Recent studies have explored the utilization of tumor-specific microenvironments pH-sensitive to create inorganic nanoparticles to improve drug delivery. These instances include Maryam Zoghi et al. who used multilayered shell-nucleus structures to target human breast cancer cell line MCF-7 for *in vitro* cancer cell diagnostic and therapeutic efficacy [45]. And Faranak Aghaz et al., using serine as a charge reversal template developed a pH-responsive sericin to carry out cellular uptake and cytotoxicity studies on human breast cancer MCF-7 cells [46]. These experiments demonstrate the potential of exploiting the weakly acidic state of the tumor microenvironment to achieve pH-responsive drug

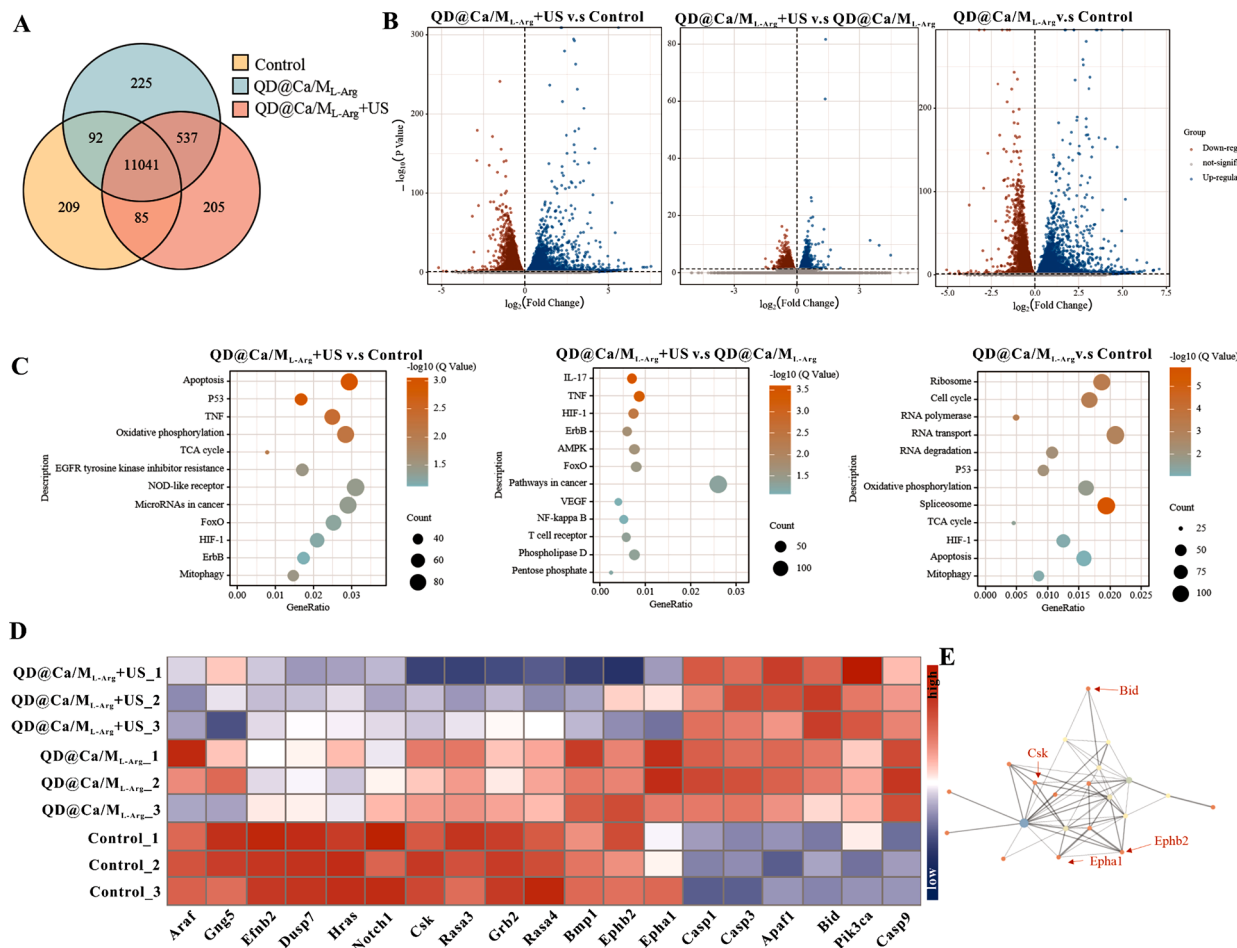


Fig. 8. Venn diagram of whole gene transcription (A); volcano plots displayed the genic expression (B); KEGG pathway enrichment analysis (C); Heat map of interest genes' transcription (D); Protein–protein interaction networks were depicted based on STRING database (E).

release and *in vitro* cancer therapy.

In this study, we referenced the SDT properties of Ag₂S and constructed a CaCO₃ nanoscale drug delivery system for TME-response modulation. The combination therapy of SDT, Ca²⁺-interference therapy and NO gas therapy produced excellent therapeutic effects on cancer cells. Meanwhile, the TME response and modulation were skillfully combined to achieve immunosuppressive reprogramming. The experimental results indicate that this design has high potential in cancer therapy and unique advantages in activating anti-tumor immunity. Compared with conventional chemotherapeutic drugs, ultrasound as a non-invasive treatment method is avoided from drug toxicity and other toxic damage. In addition, the ultrasound-triggered nanoplateform combined with TME modulation achieves equivalent therapeutic effect as chemotherapeutic drugs.

However, the application of nanoscale drug delivery system-based clinical surgical therapies is still in the initial stage of adjuvant therapy, due to the delivery mode and long-term biosafety assessment are not yet fully clarified. To promote the application of nano-pharmaceutical therapy in clinical translation, the issues still need to be addressed: a) The *in vitro* system applied in the project with the limitation of lacking the principle of biological wholeness, and the integrity needs to be optimized urgently; b) regarding the components and intricate interactions of TME, there is still multitudinous work to be carried. And there are deficiencies in our understanding of TME as well; c) issues as *in vivo* circulation and metabolism, and biological toxicity assessment are expected to be resolved.

CRediT authorship contribution statement

Jiale Cai: Methodology, Investigation, Data curation, Writing – original draft. **Guiping Hu:** Methodology, Formal analysis. **Lihua Hu:** Methodology, Formal analysis. **Junge Chen:** Methodology, Formal analysis. **Dan Chen:** Investigation, Data curation. **Dan Liu:** Investigation, Data curation. **Xiaolei Wang:** Investigation, Data curation. **Boxian Hu:** Investigation, Data curation. **Cheng Li:** Conceptualization, Methodology, Supervision, Data curation, Funding acquisition, Writing – review & editing.

Declaration of Competing Interest

The authors declare that they have no known competing financial interests or personal relationships that could have appeared to influence the work reported in this paper.

Acknowledgements

This research was supported by the National Natural Science Foundation of China Nos. 82001848, and the Fundamental Research Funds for the Central Universities NOS. YWF-21-BJ-J-1169, YWF-22-L-1169 and YWF-23-YG-QB-031.

Supplementary materials

Supplementary material associated with this article can be found, in the online version, at [doi:10.1016/j.tranon.2023.101771](https://doi.org/10.1016/j.tranon.2023.101771).

References

- [1] F. Bray, J. Ferlay, I. Soerjomataram, R.L. Siegel, L.A. Torre, A. Jemal, Global cancer statistics 2018: GLOBOCAN estimates of incidence and mortality worldwide for 36 cancers in 185 countries, CA Cancer J. Clin. 68 (2018) 394–424, <https://doi.org/10.3322/caac.21492>.
- [2] T. Ji, Y. Zhao, Y. Ding, G. Nie, Using functional nanomaterials to target and regulate the tumor microenvironment: diagnostic and therapeutic applications, Adv. Mater. 25 (2013) 3508–3525, <https://doi.org/10.1002/adma.201300299>.
- [3] T. Sun, Y.S. Zhang, B. Pang, D.C. Hyun, M. Yang, Y. Xia, Engineered nanoparticles for drug delivery in cancer therapy, Angew. Chem. Int. Ed. 53 (2014) 12320–12364, <https://doi.org/10.1002/anie.201403036>.
- [4] H. Phuengkham, L. Ren, I.W. Shin, Y.T. Lim, Nanoengineered immune niches for reprogramming the immunosuppressive tumor microenvironment and enhancing cancer immunotherapy, Adv. Mater. 31 (2019), 1803322, <https://doi.org/10.1002/adma.201803322>.
- [5] E. Boedtkjer, S.F. Pedersen, The acidic tumor microenvironment as a driver of cancer, Annu. Rev. Physiol. 82 (2020) 103–126, <https://doi.org/10.1146/annurev-physiol-021119-034627>.
- [6] R.A. Cairns, I.S. Harris, T.W. Mak, Regulation of cancer cell metabolism, Nat. Rev. Cancer 11 (2011) 85–95, <https://doi.org/10.1038/nrc2981>.
- [7] R.A. Cardone, S.J. Casavola V Fau - Reskin, S.J. Reskin, C. Nat Rev, The role of disturbed pH dynamics and the Na⁺/H⁺ exchanger in metastasis, Nat. Rev. Cancer 5 (2005).
- [8] P. Sonveaux, F. Végran, T. Schroeder, M.C. Wergin, J. Verrax, Z.N. Rabbani, C.J. De Saedeleer, K.M. Kennedy, C. Diepart, B.F. Jordan, M.J. Kelley, B. Gallez, M.L. Wahl, O. Feron, M.W. Dewhirst, Targeting lactate-fueled respiration selectively kills hypoxic tumor cells in mice, J. Clin. Invest. 118 (2008) 3930–3942, <https://doi.org/10.1172/JCI36843>.
- [9] N. Raghunand, X. He, R. van Sluis, B. Mahoney, B. Baggett, C.W. Taylor, G. Paine-Murrieta, D. Roe, Z.M. Bhujwalla, R.J. Gillies, Enhancement of chemotherapy by manipulation of tumour pH, Br. J. Cancer 80 (1999) 1005–1011, <https://doi.org/10.1038/sj.bjc.6690455>.
- [10] Z. Ge, S. Liu, Functional block copolymer assemblies responsive to tumor and intracellular microenvironments for site-specific drug delivery and enhanced imaging performance, Chem. Soc. Rev. 42 (2013) 7289–7325, <https://doi.org/10.1039/C3CS60048C>.
- [11] X. Wang, X. Zhong, J. Li, Z. Liu, L. Cheng, Inorganic nanomaterials with rapid clearance for biomedical applications, Chem. Soc. Rev. 50 (2021) 8669–8742, <https://doi.org/10.1039/D0CS00461H>.
- [12] C. Wang, Z. Dong, Y. Hao, Y. Zhu, J. Ni, Q. Li, B. Liu, Y. Han, Z. Yang, J. Wan, K. Yang, Z. Liu, L. Feng, Coordination polymer-coated CaCO₃ reinforces radiotherapy by reprogramming the immunosuppressive metabolic microenvironment, Adv. Mater. 34 (2022), 2106520, <https://doi.org/10.1002/adma.202106520>.
- [13] L. Xu, G. Tong, Q. Song, C. Zhu, H. Zhang, J. Shi, Z. Zhang, Enhanced intracellular Ca²⁺ nanogenerator for tumor-specific synergistic therapy via disruption of mitochondrial Ca²⁺ homeostasis and photothermal therapy, ACS Nano 12 (2018) 6806–6818, <https://doi.org/10.1021/acsnano.8b02034>.
- [14] P. Yang, Y. Chang, J. Zhang, F. Gao, X. Liu, Q. Wei, X. Ma, Y. Guo, The combination of *in situ* photodynamic promotion and ion-interference to improve the efficacy of cancer therapy, J. Colloid Interface Sci. 629 (2023) 522–533, <https://doi.org/10.1016/j.jcis.2022.08.125>.
- [15] J. Zhu, A. Jiao, Q. Li, X. Lv, X. Wang, X. Song, B. Li, Y. Zhang, X. Dong, Mitochondrial Ca²⁺-overloading by oxygen/glutathione depletion-boosted photodynamic therapy based on a CaCO₃ nanoplateform for tumor synergistic therapy, Acta Biomater. 137 (2022) 252–261, <https://doi.org/10.1016/j.actbio.2021.10.016>.
- [16] J. Xie, Y. Wang, W. Choi, P. Jangili, Y. Ge, Y. Xu, J. Kang, L. Liu, B. Zhang, Z. Xie, J. He, N. Xie, G. Nie, H. Zhang, J.S. Kim, Overcoming barriers in photodynamic therapy harnessing nano-formulation strategies, Chem. Soc. Rev. 50 (2021) 9152–9201, <https://doi.org/10.1039/D0CS01370F>.
- [17] Z.A.O. Gong, Z.A.O. Dai, S. Adv, Design and challenges of sonodynamic therapy system for cancer theranostics: from equipment to sensitizers, Adv. Sci. (2021).
- [18] Y. Yang, B.Z. Chen, X.P. Zhang, H. Zheng, Z. Li, C.Y. Zhang, X.D. Guo, Conductive microneedle patch with electricity-triggered drug release performance for atop dermatitis treatment, ACS Appl. Mater. Interfaces 14 (2022) 31645–31654, <https://doi.org/10.1021/acsmami.2c05952>.
- [19] S. Stapleton, M. Dunne, M. Milosevic, C.W. Tran, M.J. Gold, A. Vedadi, T.D. McKee, P.S. Ohashi, C. Allen, D.A. Jaffray, Radiation and heat improve the delivery and efficacy of nanotherapeutics by modulating intratumoral fluid dynamics, ACS Nano 12 (2018) 7583–7600, <https://doi.org/10.1021/acsnano.7b06301>.
- [20] J. Yu, F. Zhao, W. Gao, X. Yang, Y. Ju, L. Zhao, W. Guo, J. Xie, X. Liang, X. Tao, J. Li, Y. Ying, W. Li, J. Zheng, L. Qiao, S. Xiong, X. Mou, S. Che, Y. Hou, Magnetic reactive oxygen species nanoreactor for switchable magnetic resonance imaging guided cancer therapy based on pH-Sensitive Fe₅C₂@Fe₃O₄ nanoparticles, ACS Nano 13 (2019) 10002–10014, <https://doi.org/10.1021/acsnano.9b01740>.
- [21] D. Li, Y. Yang, D. Li, J. Pan, C. Chu, G. Liu, Organic sonosensitizers for sonodynamic therapy: from small molecules and nanoparticles toward clinical development, Small 17 (2021), 2101976, <https://doi.org/10.1002/smll.202101976>.
- [22] X. Pan, H. Wang, S. Wang, X. Sun, L. Wang, W. Wang, H. Shen, H. Liu, Sonodynamic therapy (SDT): a novel strategy for cancer nanotheranostics, Sci. China Life Sci. 61 (2018) 415–426, <https://doi.org/10.1007/s11427-017-9262-x>.
- [23] S.S. Sabharwal, P.T. Schumacker, Mitochondrial ROS in cancer: initiators, amplifiers or an Achilles' heel? Nat. Rev. Cancer 14 (2014) 709–721, <https://doi.org/10.1038/nrc3803>.
- [24] Q. Zhang, C. Bao, X. Cai, L. Jin, L. Sun, Y. Lang, L. Li, Sonodynamic therapy-assisted immunotherapy: a novel modality for cancer treatment, Cancer Sci. 109 (2018) 1330–1345, <https://doi.org/10.1111/cas.13578>.
- [25] T. Inui, K. Makita, H. Miura, A. Matsuda, D. Kuchiike, K. Kubo, M. Mette, Y. Uto, T. Nishikata, H. Horii, N. Sakamoto, Case report: a breast cancer patient treated with GcMAF, sonodynamic therapy and hormone therapy, Anticancer Res. 34 (2014) 4589. <http://ar.iiarjournals.org/content/34/8/4589.abstract>.
- [26] Y. Wan, L.H. Fu, C. Li, J. Lin, P. Huang, Conquering the hypoxia limitation for photodynamic therapy, Adv. Mater. 33 (2021), 2103978, <https://doi.org/10.1002/adma.202103978>.

- [27] X. Liang, M. Chen, P. Bhattacharai, S. Hameed, Z. Dai, Perfluorocarbon@porphyrin nanoparticles for tumor hypoxia relief to enhance photodynamic therapy against liver metastasis of colon cancer, *ACS Nano* 14 (2020) 13569–13583, <https://doi.org/10.1021/acsnano.0c05617>.
- [28] H. Chen, C. He, T. Chen, X. Xue, New strategy for precise cancer therapy: tumor-specific delivery of mitochondria-targeting photodynamic therapy agents and *in situ* O₂-generation in hypoxic tumors, *Biomater. Sci.* 8 (2020) 3994–4002, <https://doi.org/10.1039/DOBM00500B>.
- [29] Y. Wang, J. Yu, Z. Luo, Q. Shi, G. Liu, F. Wu, Z. Wang, Y. Huang, D. Zhou, Engineering endogenous tumor-associated macrophage-targeted biomimetic nano-RBC to reprogram tumor immunosuppressive microenvironment for enhanced chemo-immunotherapy, *Adv. Mater.* 33 (2021), 2103497, <https://doi.org/10.1002/adma.202103497>.
- [30] J.O. Lundberg, E. Weitzberg, Nitric oxide signaling in health and disease, *Cell* 185 (2022) 2853–2878, <https://doi.org/10.1016/j.cell.2022.06.010>.
- [31] D. Fukumura, S. Kashiwagi, R.K. Jain, The role of nitric oxide in tumour progression, *Nat. Rev. Cancer* 6 (2006) 521–534, <https://doi.org/10.1038/nrc1910>.
- [32] P. Pacher, J.S. Beckman, L. Liaudet, Nitric oxide and peroxynitrite in health and disease, *Physiol. Rev.* 87 (2007) 315–424, <https://doi.org/10.1152/physrev.00029.2006>.
- [33] M. Shi, J. Zhang, Y. Wang, C. Peng, H. Hu, M. Qiao, X. Zhao, D. Chen, Tumor-specific nitric oxide generator to amplify peroxynitrite based on highly penetrable nanoparticles for metastasis inhibition and enhanced cancer therapy, *Biomaterials* 283 (2022), 121448, <https://doi.org/10.1016/j.biomaterials.2022.121448>.
- [34] S. Shiva, P.S. Brookes, R.P. Patel, P.G. Anderson, V.M. Darley-Usmar, Nitric oxide partitioning into mitochondrial membranes and the control of respiration at cytochrome c oxidase, *Proc. Natl Acad. Sci.* 98 (2001) 7212–7217, <https://doi.org/10.1073/pnas.131128898>.
- [35] W. Tang, Z. Yang, L. He, L. Deng, P. Fathi, S. Zhu, L. Li, B. Shen, Z. Wang, O. Jacobson, J. Song, J. Zou, P. Hu, M. Wang, J. Mu, Y. Cheng, Y. Ma, L. Tang, W. Fan, X. Chen, A hybrid semiconducting organosilica-based O₂ nanoeconomizer for on-demand synergistic photothermally boosted radiotherapy, *Nat. Commun.* 12 (2021) 523, <https://doi.org/10.1038/s41467-020-20860-3>.
- [36] C. Li, X.Q. Yang, J. An, K. Cheng, X.L. Hou, X.S. Zhang, Y.G. Hu, B. Liu, Y.D. Zhao, Red blood cell membrane-enveloped O₂ self-supplementing biomimetic nanoparticles for tumor imaging-guided enhanced sonodynamic therapy, *Theranostics* 10 (2020) 867–879, <https://doi.org/10.7150/thno.37930>.
- [37] Z. Dong, L. Feng, Y. Hao, M. Chen, M. Gao, Y. Chao, H. Zhao, W. Zhu, J. Liu, C. Liang, Q. Zhang, Z. Liu, Synthesis of hollow biominerализed CaCO₃-polydopamine nanoparticles for multimodal imaging-guided cancer photodynamic therapy with reduced skin photosensitivity, *J. Am. Chem. Soc.* 140 (2018) 2165–2178, <https://doi.org/10.1021/jacs.7b11036>.
- [38] J.L. Wu, C.Q. Wang, R.X. Zhuo, S.X. Cheng, Multi-drug delivery system based on alginate/calcium carbonate hybrid nanoparticles for combination chemotherapy, *Colloids Surf. B Biointerfaces* 123 (2014) 498–505, <https://doi.org/10.1016/j.colsurfb.2014.09.047>.
- [39] M.Y. Qin, X.Q. Yang, K. Wang, X.S. Zhang, J.T. Song, M.H. Yao, D.M. Yan, B. Liu, Y. D. Zhao, *In vivo* cancer targeting and fluorescence-CT dual-mode imaging with nanoprobe based on silver sulfide quantum dots and iodinated oil, *Nanoscale* 7 (2015) 19484–19492, <https://doi.org/10.1039/C5NR05620A>.
- [40] Z. Dong, L. Feng, Y. Hao, Q. Li, M. Chen, Z. Yang, H. Zhao, Z. Liu, Synthesis of CaCO₃-based nanomedicine for enhanced sonodynamic therapy via amplification of tumor oxidative stress, *Chem* 6 (2020) 1391–1407, <https://doi.org/10.1016/j.chempr.2020.02.020>.
- [41] T. Wong, Studies on creatine determination by α -naphthol-diacetyl reaction, *Anal. Biochem.* 40 (1971) 18–28, [https://doi.org/10.1016/0003-2697\(71\)90079-0](https://doi.org/10.1016/0003-2697(71)90079-0).
- [42] A.D. Garg, P. Agostinis, Cell death and immunity in cancer: from danger signals to mimicry of pathogen defense responses, *Immunol. Rev.* 280 (2017) 126–148, <https://doi.org/10.1111/imr.12574>.
- [43] M. Sylvestre, C.A. Crane, S.H. Pun, Progress on modulating tumor-associated macrophages with biomaterials, *Adv. Mater.* 32 (2020), 1902007, <https://doi.org/10.1002/adma.201902007>.
- [44] M. Cieslik, A.M. Chinnaiyan, Cancer transcriptome profiling at the juncture of clinical translation, *Nat. Rev. Genet.* 19 (2018) 93–109, <https://doi.org/10.1038/nrg.2017.96>.
- [45] M. Zoghi, M. Pourmadadi, F. Yazdian, M.N. Nigjeh, H. Rashedi, R. Sahraeian, Synthesis and characterization of chitosan/carbon quantum dots/Fe2O3 nanocomposite comprising curcumin for targeted drug delivery in breast cancer therapy, *Int. J. Biol. Macromol.* (2023), 125788, <https://doi.org/10.1016/j.ijbiomac.2023.125788>.
- [46] F. Aghaz, Z. Asadi, S. Sajadimajd, K. Kashfi, E. Arkan, Z. Rahimi, Codelivery of resveratrol melatonin utilizing pH responsive sericin based nanocarriers inhibits the proliferation of breast cancer cell line at the different pH, *Sci. Rep.* 13 (2023) 11090, <https://doi.org/10.1038/s41598-023-37668-y>.